Calculating electron transport coefficients of disordered alloys using the KKR-CPA method and Boltzmann approach: Application to $Mg_2Si_{1-x}Sn_x$ thermoelectrics

K. Kutorasiński, J. Tobola, and S. Kaprzyk

AGH University of Science and Technology, Faculty of Physics and Applied Computer Science, Al. Mickiewicza 30, 30-059 Krakow, Poland

(Received 17 January 2013; revised manuscript received 15 April 2013; published 15 May 2013)

Electronic band-structure calculations combined with the Boltzmann transport approach are implemented to determine temperature-dependent electron-transport properties such as electrical conductivity $\sigma(T)$, thermopower $S(T)$, electronic thermal conductivity $\kappa_e(T)$, and related quantities such as the Lorenz number $L(T)$ and the power factor $PF(T)$. The Korringa-Kohn-Rostoker method with the coherent potential approximation (KKR-CPA) is employed to study the electronic structure of a chemically disordered system and also to explore the Fermi surface. This allows for the determination of the velocity and lifetime of an electron. The aforementioned procedure was then applied to investigate promising n-doped $Mg_2Si_{1-x}Sn_x$ thermoelectric material. Using different approaches for relaxation time as well as treating the lattice thermal conductivity κ_l as an adjustable parameter, the thermoelectric figure of merit, ZT, was calculated in terms of temperature T and carrier concentration n. The $ZT(n,T)$ map for $Mg_2Si_{1-x}Sn_x$ clearly shows that, for an experimental value of $\kappa_l \sim 1.25$ W m^{-1} K^{-1}, the strongest thermoelectric properties are expected for $x \sim 0.6$ composition, when two conduction bands tend to degenerate near the X point. On the whole, the KKR-CPA results well correspond to experimental findings upon employing the constant-relaxation-time approach, especially concerning thermopower $S(T)$. The above-mentioned method was also used to estimate the figure of merit of a hypothetical nanograin material with low thermal conductivity ($\kappa_l \sim 0.5$ W m^{-1} K^{-1}), yielding $ZT \sim 2$.

DOI: 10.1103/PhysRevB.87.195205 PACS number(s): 71.18.+y, 71.23.−k, 72.15.Lh, 72.20.Pa

I. INTRODUCTION

The study of electronic and thermal transport properties of solid-state materials has always been a difficult problem for condensed-matter theory due to the complexity of the phenomena that should be taken into account. The most convenient and recently explored way is based on density functional theory (DFT) electronic band-structure calculations combined with the Boltzmann transport theory.[1–4] Actually, the electronic band structure, together with the known number of electrons in the system, defining the Fermi surface, contains information on ground-state properties. In addition, temperature effects can be incorporated into such computations through the Fermi-Dirac distribution function. On the other hand, to get a more complete set of information on electron-transport behaviors (or electron scattering) in a system, the relaxation time of electrons on bands lying in the vicinity of the Fermi energy (E_F) is needed. In practice, calculation of the relaxation time remains a hard task[5,6] and in most cases it must be approximated and parametrized.

In this paper, the Korringa-Kohn-Rostoker (KKR)[7–9] method based on the Green's function multiple scattering theory was used to calculate electronic band structure and relevant kinetic parameters of electrons in the vicinity of E_F. Moreover, the coherent potential approximation (CPA) was employed both to account for chemical disorder effects on electronic structure[10–13] and to determine the electron's lifetime connected with scattering by the impurities.[14,15] In general, the relaxation time contains information about all possible scattering mechanisms; however, owing to Matthiessen's rule, when one mechanism dominates, other ones can be separated or even neglected. Hence, when electrical conductivity is mostly driven by chemical disorder, like in alloys, scattering on impurity remains the key mechanism of electron diffusion, and the KKR-CPA method appears to be a well-adapted technique for retrieving the information required for calculating the electron-transport coefficients without any adjustable parameter.

In this paper the linearized Boltzmann equation is implemented to calculate electron-transport coefficients such as electrical conductivity σ, Seebeck coefficient S, the electronic part of thermal conductivity, κ_e, and the effective Lorentz number[16] L. As an illustrative example, this procedure was applied to the promising n-type $Mg_2Si_{1-x}Sn_x$ thermoelectric material, which is intensively investigated[17–19] both experimentally and theoretically due to the so-called conduction-band convergence.[20–23]

The paper is organized as follows. Section II presents theoretical details of electron-transport-coefficient calculations in terms of transport function. Different approximations were employed for the electron-scattering mechanism, i.e., constant relaxation time τ, constant mean free path λ, and constant mobility μ. Moreover, relaxation time, which is treated as a free parameter, was extracted from experimental data for further calculations. In Sec. III the details of the application of the method in $Mg_2Si_{1-x}Sn_x$ are discussed. Section IV reports the computational results of the temperature-dependent transport properties, i.e., $\sigma(T)$, $S(T)$, and $\kappa_e(T)$, within the above-mentioned models of electron scattering. This section also discusses maps of the power factor $PF(n,T) = S^2\sigma$, the effective Lorenz number $L = \kappa_e/(\sigma T)$, and the figure of merit, $ZT(n,T) = \sigma S^2/\kappa$ (with $\kappa = \kappa_e + \kappa_l$), versus electron concentration n and temperature T, assuming arbitrary values of lattice thermal conductivity κ_l. The paper is concluded in Sec. V. The Appendix details the relationship between nominal and active concentrations, which is important to account for an appropriate comparison between theoretical and experimental values.

II. THEORETICAL DETAILS

A convenient way to extract transport coefficients in the semiclassical approach is Boltzmann theory. On the basis of electronic band structure and lifetime of electrons it is possible to calculate transport coefficients (σ, S, and κ_e). They can be defined in compact form in terms of $\mathscr{L}^{(\alpha)}$ functions,[16]

$$\begin{aligned} \boldsymbol{\sigma}_e &= \mathscr{L}^{(0)}, \quad \boldsymbol{S} = -\frac{1}{eT}\frac{\mathscr{L}^{(1)}}{\mathscr{L}^{(0)}}, \\ \boldsymbol{\kappa_e} &= \frac{\mathscr{L}^{(2)}}{e^2T} - \frac{\mathscr{L}^{(1)}\mathscr{L}^{(1)}}{e^2T\mathscr{L}^{(0)}}, \end{aligned} \tag{1}$$

where

$$\mathscr{L}^{(\alpha)} = \int d\mathscr{E}\left(-\frac{\partial f}{\partial \mathscr{E}}\right)(\mathscr{E}-\mu_c)^{\alpha}\boldsymbol{\sigma}(\mathscr{E}). \tag{2}$$

The latter contains the central quantity of the Boltzmann theory, i.e., the $\boldsymbol{\sigma}(\mathscr{E})$ tensor, which is usually called the transport function. The transport function $\boldsymbol{\sigma}(\mathscr{E})$ together with the chemical potential μ_c appear to be necessary data for performing a calculation of thermoelectric coefficients.

A. Transport function and approximations

The most critical part is the calculation of the transport tensor $\boldsymbol{\sigma}(\mathscr{E})$, which contains the information of the electronic band structure and the relaxation time. In general, it has a tensor form

$$\boldsymbol{\sigma}(\mathscr{E}) = e^2\sum_n \int \frac{d\mathbf{k}}{4\pi^3}\tau_n(\mathbf{k})\mathbf{v}_n(\mathbf{k})\otimes\mathbf{v}_n(\mathbf{k})\delta(\mathscr{E}-\mathscr{E}_n(\mathbf{k})), \tag{3}$$

where $\mathscr{E}_n(\mathbf{k})$ are band energies, and $\tau_n(\mathbf{k})$ and $\mathbf{v}_n(\mathbf{k})$ denote an electron's lifetime and velocity, respectively. The latter can be determined from a k-space gradient $\mathbf{v}_n(\mathbf{k}) = 1/\hbar\nabla_k\mathscr{E}_n(\mathbf{k})$. All these quantities are assigned the specific band n. In Eq. (3) k-space integration runs over the Brillouin zone (BZ) and summation over all bands. For convenience, the k-space volume is integrated over isoenergetic surfaces $S_n(\mathscr{E})$ using the formula

$$\int d\mathbf{k}\delta(\mathscr{E}-\mathscr{E}(\mathbf{k})) = \int_{S(\mathscr{E})}\frac{dS}{|\nabla_k\mathscr{E}_n(\mathbf{k})|}. \tag{4}$$

The velocity $\mathbf{v}_n(\mathbf{k})$ can be calculated directly from $\mathscr{E}_n(\mathbf{k})$, which is commonly extracted from most periodic DFT-based codes for electronic structure calculations. Electron lifetime $\tau(S_n(\mathscr{E}))$ is usually not calculated but instead is treated as a free parameter. More generally speaking, relaxation time τ may describe different scattering phenomena, which are not explicitly included in periodic DFT calculations. Accordingly, few approximations were applied to examine their effect on transport function and relevant electron-transport coefficients. We have considered the following cases.

Constant lifetime. In this case, τ does not depend on $\mathbf{k}$ or even on energy and $\tau_0 = \tau(S_n(\mathscr{E}))$ becomes a parameter:

$$\boldsymbol{\sigma}_\tau(\mathscr{E}) = \tau_0\frac{e^2}{\hbar}\sum_n\int_{S_n(\mathscr{E})}\frac{dS}{4\pi^3}\frac{\mathbf{v}(S_n(\mathscr{E}))\otimes\mathbf{v}(S_n(\mathscr{E}))}{|\mathbf{v}(S_n(\mathscr{E}))|}. \tag{5}$$

Constant mean free path. In this case, λ as a product of velocity and lifetime at each $\mathbf{k}$ point is constant and $\lambda_0 = |\mathbf{v}(S_n(\mathscr{E}))|\tau(S_n(\mathscr{E}))$ becomes a parameter:

$$\boldsymbol{\sigma}_\lambda(\mathscr{E}) = \lambda_0\frac{e^2}{\hbar}\sum_n\int_{S_n(\mathscr{E})}\frac{dS}{4\pi^3}\frac{\mathbf{v}(S_n(\mathscr{E}))\otimes\mathbf{v}(S_n(\mathscr{E}))}{|\mathbf{v}(S_n(\mathscr{E}))|^2}. \tag{6}$$

Constant electron mobility. The charge carrier mobility, defined as $e\tau\langle\mathbf{v}^2\rangle/3k_BT$, does not depend on energy and $\mu_0 = e\tau(S_n(\mathscr{E}))\mathbf{v}(S_n(\mathscr{E}))^2/3k_BT$ is treated as a parameter. This approximation is accurately defined in low-doped semiconductors, whereas for heavy doping the definition is modified by the η factor (see the Appendix). It is noteworthy that this approximation also assumes direction-independent properties (as in cubic crystal), and tensors become scalar functions. Consequently, it yields the following expression for the transport function:

$$\begin{aligned} \sigma_\mu(\mathscr{E}) &= \frac{e^2\tau\langle\mathbf{v}^2\rangle}{3}\sum_n\int_{S_n(\mathscr{E})}\frac{dS}{4\pi^3}\frac{1}{|\nabla_k\mathscr{E}_n(\mathbf{k})|} \\ &= e\frac{\mu_0}{\eta}k_BTg(\mathscr{E}), \end{aligned} \tag{7}$$

where $g(\mathscr{E})$ denotes the density of states (DOS) function.

It is worth mentioning that, within all these approximations, the free parameters cancel out when the Seebeck coefficient S and the effective Lorenz number L are calculated. On the contrary, these parameters must be fitted while charge and thermal conductivities (σ and κ_e) are computed.

B. Beyond constant-relaxation-time approximation

In the case of alloys, CPA allows calculation of not only the real part of the energy band but also its imaginary part, which gives the lifetime of an electron[14,24] $\tau_{\mathrm{cp}}(\mathbf{k}) = \hbar/(2\,\mathrm{Im}\,\mathscr{E}(\mathbf{k}))$. When derived in such a way, the lifetime corresponds to scattering on impurity and, using Matthiessen's rule, it can be added to the constant parameter τ_{other} (corresponding to other scattering mechanisms), which gives the following expression:

$$\tau(\mathbf{k}) = \left(\frac{1}{\tau_{\mathrm{cp}}(\mathbf{k})} + \frac{1}{\tau_{\mathrm{other}}}\right)^{-1} \tag{8}$$

It is worth noting that by taking into account only the CPA lifetime τ_{cp} (when $\tau_{\mathrm{other}} = 0$), the electrical resistivity related to impurities can be found, especially in the limit $T \to 0$, yielding residual resistivity determined with no adjustable parameter.

The average lifetime as a function of energy is determined using the formula

$$\langle\tau(\mathscr{E})\rangle = \sum_n\frac{\int_{S_n(\mathscr{E})}dS\;\tau(S_n(\mathscr{E}))|\mathbf{v}(S_n(\mathscr{E}))|}{\int_{S_n(\mathscr{E})}dS|\mathbf{v}(S_n(\mathscr{E}))|}. \tag{9}$$

C. Chemical potential

Chemical potential $\mu_c = \mu_c(T,n_d)$ is calculated using the DOS function for a known number of electrons per unit cell n in the system smeared by Fermi-Dirac distribution (to mimic temperature effect) as follows:

$$n + n_d = \int d\mathscr{E}\,g(\mathscr{E})\frac{1}{1+e^{\frac{\mathscr{E}-\mu_c(T,n_d)}{k_BT}}}. \tag{10}$$

In Eq. (10), n_d is an additional carrier concentration corresponding to a small number of doped electrons (e.g., Sb in $Mg_2Si_{1-x}Sn_x$). For a very low content of dopants a rigid-band model[25] seems to be valid, except for particular cases when DOS near valence- or conduction-band edges is strongly modified by introduced impurities (e.g., resonantlike levels[26]).

III. APPLICATION TO Mg_2(Si-Sn)

A. Structural aspects and computational details

Mg_2Si ($a = 6.100$ Å) and Mg_2Sn ($a = 6.345$ Å) crystallize in the fcc antifluorite-type structure (space group $Fm\bar{3}m$) and exhibit semiconducting properties. The $Mg_2Si_{1-x}Sn_x$ alloy preserves the same crystal structure, excluding the $0.4 < x < 0.6$ concentration range where presumably a two-phase region was detected.[20] The lattice constant increases linearly with Sn content increase. On the whole, the Sn-rich alloys have rather low ZT (below 0.2); however, after doping on the Si/Sn site with Sb or Bi, for example, the thermoelectric figure of merit may increase up to $ZT = 1$ at 700 K in $Mg_2Si_{0.3}Sn_{0.7}$:Sb.[27]

The $Mg_2Si_{1-x}Sn_x$ system was selected for calculation due to the unusual features of the band structure presumably driving high ZT. The most interesting concentration range corresponds to $x = 0.5$–0.7, where two conduction bands strongly change near the point X in the BZ; i.e., they mutually shift on the energy scale to degenerate at a critical x content.[20–22] Electronic band-structure calculations were performed by the KKR-CPA method. The crystal potential of the muffin-tin form was constructed in the framework of the local density approximation (LDA) using the Barth-Hedin[28] form for exchange-correlation potential. The self-consistency cycles were repeated until the maximum difference between the input and output potentials was less than 1 mRy in any mesh point in the unit cell. The generalized Lloyd formula[29] was employed to compute the Fermi level and total DOS directly from the Green function.[12] In order to verify the effect of the spherical form of the potential on $\mathscr{E}_n(\mathbf{k})$, full-potential KKR calculations were also performed for the parent compounds Mg_2Si and Mg_2Sn. The shape of the conduction bands was found to be negligibly affected. Conversely, the role of relativistic effects, e.g., the spin-orbit coupling in the calculation of electron transport coefficients, especially in the case of Sn-rich alloys, is more critical. The question was addressed via the fully relativistic KKR method, which resulted in strong spin-orbit splitting of valence bands in the vicinity of the X point. Fortunately, the conduction bands, a subject of our theoretical investigations, appeared not to be sensitive. Another important point corresponds to the LDA limit in computations of the band gap E_g. A very recent linearized augmented plane wave calculation[30] of $Mg_2Si_{0.5}Sn_{0.5}$ revealed that employing a more sophisticated exchange-correlation potential (e.g., (TB-mBJ)[31]) resulted in the correct value of E_g. Since the gap's magnitude has an important effect on the shape of the $\sigma(T)$, $S(T)$, and $\kappa_e(T)$ curves (especially at high temperature), it is important for the gap to have a good value so as to reasonably estimate ZT versus temperature and carrier concentration. Accordingly, the separation between conduction and valence bands $\mathscr{E}_n(\mathbf{k})$ computed in $Mg_2Si_{1-x}Sn_x$ was expanded to the experimental value (e.g., 0.3–0.4 eV for $0.5 < x < 0.7$). In addition, electronic structure calculations were performed with some previously presented technical details.[12,15]

IV. RESULTS

KKR-CPA calculations were done for three samples of $Mg_2Si_{1-x}Sn_x$: $x = 0.5$, $x = 0.6$, and $x = 0.7$. As expected for Mg_2Si, the KKR-LDA method resulted in almost twofold underestimation of E_g with respect to the experimental value, i.e., 0.3 eV versus 0.75 eV.[20,32] A small overlap of conduction and valence bands was computed in Mg_2Sn, unlike a true gap (0.35 eV). The band gaps were adjusted to the experimental value.[20] The isoenergetic surfaces $S(\mathscr{E})$ needed in Eq. (4) were determined using the marching cube algorithm[33] with an $80 \times 80 \times 80$ box in the BZ. The surfaces were reproduced by a set of triangles and in the case of n- and p-type $Mg_2Si_{0.4}Sn_{0.6}$ (Fig. 1) the plotted Fermi surfaces consisted of ~15 000 and ~12 000 triangles, respectively. All energy-dependent functions were calculated with 3-meV resolution and interpolated by cubic spline functions. The chemical potential and all transport coefficients were computed in the temperature range 10–800 K and in the concentration range 10^{19}–10^{21} cm^{-3} for both types of carriers. The integral [Eq. (10)] was solved iteratively to extract $\mu_c(T,n_d)$ with high precision. It is worth noting that in $Mg_2Si_{1-x}Sn_x$ an increase of electron carrier concentration was experimentally achieved by doping with Sb or Bi (on the Si/Sn site). Additionally, via KKR-CPA (by computing self-consistently the electronic structure of $Mg_2Si_{1-x-y}Sn_xSb_y$ and $Mg_2Si_{1-x-y}Sn_xBi_y$ with $y = 0.01, 0.02, 0.03$) we verified that neither dopant practically alters an important part of the conduction bands. Finally, the Fermi level was shifted in a rigid way on the KKR-CPA bands of $Mg_2Si_{1-x}Sn_x$ to facilitate calculations of thermoelectric properties and to mimic extra electronlike doping.

A. Band structure

The calculation of transport properties requires a highly accurate electronic structure $\mathscr{E}(\mathbf{k})$. Figure 1 shows the band curves for $x = 0.6$ when the conduction bands tend to converge. The dispersion curves of $Mg_2Si_{0.5}Sn_{0.5}$ and $Mg_2Si_{0.3}Sn_{0.7}$ along high-symmetry directions are shown in Fig. 2. One can observe that at the point X, two conduction bands become upside-down when the concentration x is varied from 0.5 to 0.7. This behavior was initially predicted experimentally[20] and was later calculated from the KKR-CPA method.[22] The ΔE between two conduction bands at the point X is as small as 44 meV and 67 meV, in $x = 0.7$ and $x = 0.5$, respectively.

B. Resistivity

Electrical resistivity was calculated using three approximations (see Sec. II A). The adjustable parameters were obtained from fitting the experimental curves[20] for three different carrier concentrations in $Mg_2Si_{0.4}Sn_{0.6}$. However, the residual resistivity ($T = 0$ limit) was computed directly from the KKR-CPA, employing the lifetime attached from the imaginary part of complex energy band.

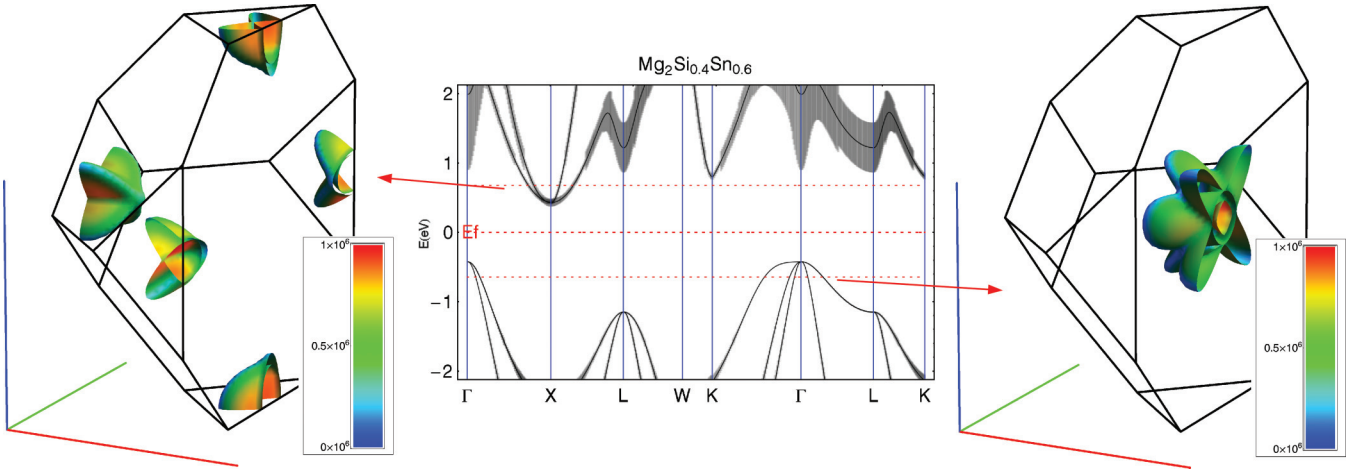

FIG. 1. (Color online) Electron bands and Fermi surfaces of $Mg_2Si_{1-x}Sn_x$. Shadows around bands represent the imaginary part of the energy, enlarged 100 times to make it visible. The Fermi surfaces are plotted for carrier concentration $n = 10^{22}$ cm^{-3} of electrons (left side) and holes (right side). The colors on the Fermi surfaces represent the velocity of electrons in ms^{-1}.

1. *Impurity resistivity*

From Fig. 3 one observes that the lifetime depending on energy and connected to scattering on impurities $[\tau_{cp}(\mathscr{E})]$ tends to infinity when approaching the gap. Impurity scattering plays a more important role away from the gap (in higher concentration and lower temperature). The same behavior is seen in Table I, where ρ_{cp} was calculated using $\tau(\mathbf{k})$ [Eq. (8)] with parameter $\tau_{other} = 0$. This type of scattering contributes the most to the resistivity at lower temperature and carrier concentration.

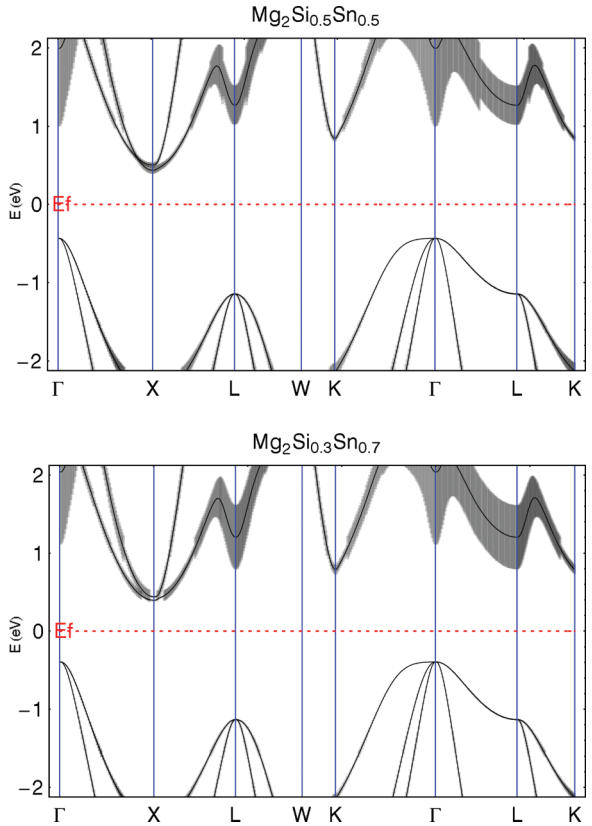

FIG. 2. (Color online) Electron bands of $Mg_2Si_{1-x}Sn_x$. Shadows around the bands represent the imaginary part of the energy (enlarged 100 times for visibility).

2. *Total resistivity*

Electrical resistivity was calculated using three transport functions as given in Eqs. (5), (6), and (7). The free parameters, i.e., lifetime τ_0, mean free path λ_0, and carrier mobility μ_0, were fitted to adjust calculated conductivity and experimental data for $Mg_2Si_{0.4}Sn_{0.6}$ measured at three different concentration as a function of temperature.[20] Matched results are shown in Fig. 4. The average of three τ_0 (Fig. 4, top) was used in further calculations of the electronic part of the thermal conductivity κ_e and thermopower S. The parameters τ_0, λ_0, and μ_0 are decreasing with temperature, which is caused mostly by increased scattering on phonons and which is not taken explicitly into account in this work.

C. Thermopower

Calculation of $S(T)$ curves was done for both n- and p-type electrical conductivity using the average of three functions of $\tau_0(T)$ (see fit in Fig. 4, top) as well as by assuming that the

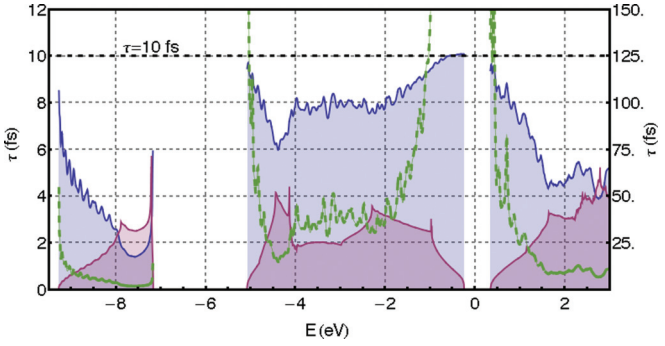

FIG. 3. (Color online) Electron lifetime $\tau(\mathscr{E})$ (solid blue line with scale on the left) for $\tau_{other} = 10$ fs [see Eq. (8)] and $\tau_{cp}(\mathscr{E})$ contribution (dashed green line with scale on the right) of $Mg_2Si_{0.4}Sn_{0.6}$. In addition, DOS function is shown (solid red line) in arbitrary units.

TABLE I. Calculated residual resistivity and its contribution to overall experimental resistivity at room and high temperature in $Mg_2Si_{0.4}Sn_{0.6}$.

Carrier concentration (cm^{-3})	Residual resistivity (Ω m)	ρ_{cp}/ρ_{expt} (%)	
		300 K	800 K
0.6×10^{20}	17.0×10^{-7}	5.4	2.4
2.5×10^{20}	5.0×10^{-7}	6.1	2.9
3.0×10^{20}	4.5×10^{-7}	8.2	4.5

lifetime does not depend on carrier concentration. Figure 5 shows that the largest thermopower is found for the lowest concentrations. The deviation from this behavior is seen only at high temperature due to the influence of activation of two types of carriers (electrons and holes), decreasing the S value.

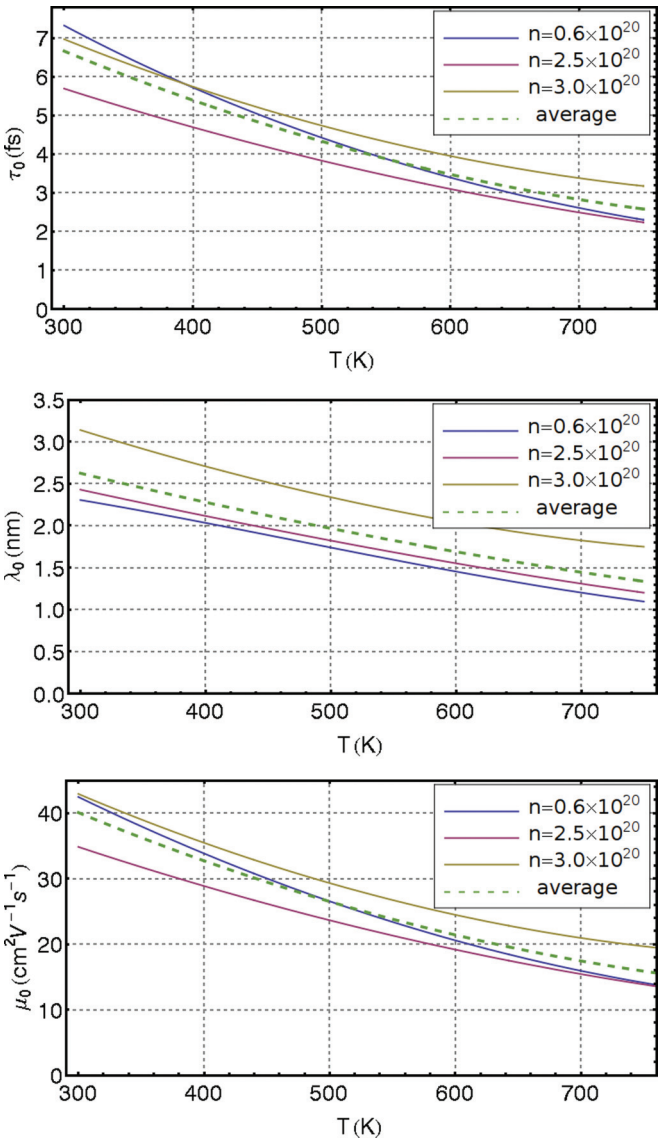

FIG. 4. (Color online) Lifetime (in fs, top) and mean free path (in nm, middle) and mobility (in $cm^2\ V^{-1}\ s^{-1}$, bottom) as a function of temperature fitted to get agreement with experiment[20] for Sb-doped $Mg_2Si_{0.4}Sn_{0.6}$. Concentration in cm^{-3}.

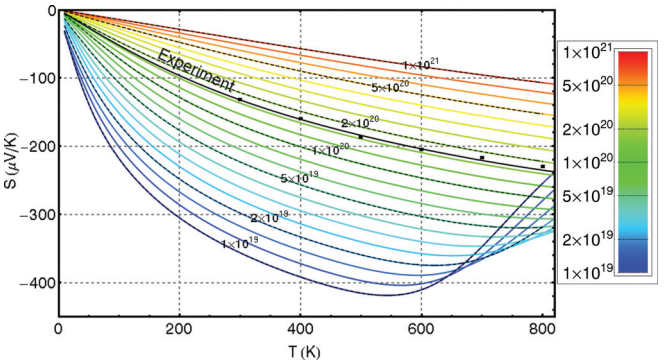

FIG. 5. (Color online) Seebeck coefficient of $Mg_2Si_{0.4}Sn_{0.6}$ as a function of temperature for different concentration. The solid black line represents concentration $n = 1.7 \times 10^{20}$ cm^{-3}. Dots show measured data[21] of Sb-doped $Mg_2Si_{0.4}Sn_{0.6}$ with carrier concentration denoted by dashed lines (concentration values given by the color in the legend).

On the whole, we observe that the experimental data[21] are very well reproduced by the constant-relaxation-time approach.

Figure 6 shows that the n-doped $Mg_2Si_{0.4}Sn_{0.6}$ alloy exhibits the largest Seebeck coefficient with respect to neighboring compositions. This behavior is well supported by the presence of the conduction-band degeneration at the point X,

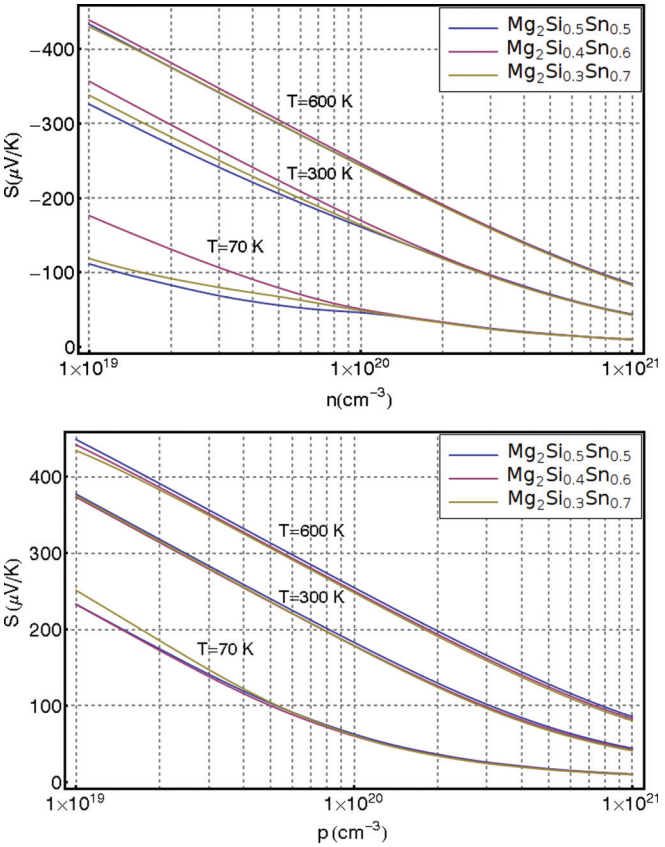

FIG. 6. (Color online) Seebeck coefficient of $Mg_2Si_{1-x}Sn_x$ as a function of carrier concentration for three different amounts of Sn and three different temperature values. The top plot represents n-type doping (i.e., Sb, Bi), and the bottom plot represents p-type doping [i.e., Ga (Ref. 34)].

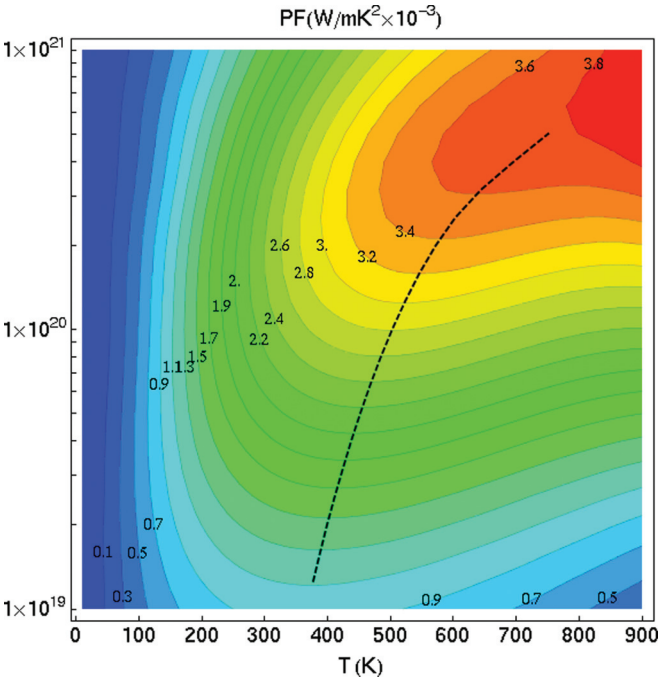

FIG. 7. (Color online) Power factor map of $Mg_2Si_{0.4}Sn_{0.6}$ as a function of temperature and nominal concentration. The dashed line represents the maximum of function $PF(T)$ for different nominal concentrations.

best seen at low temperature. At high temperature, the band splitting becomes less important (almost negligible), since $k_BT = 52$ meV for $T = 600$ K is comparable to $\Delta E \sim 44$ eV. When Sn content differs from 60% (see Fig. 2), these bands are separated more in $Mg_2Si_{0.5}Sn_{0.5}$ than in $Mg_2Si_{0.3}Sn_{0.7}$, which results in the thermopower decrease. At high concentrations, the chemical potential μ_c lies a few k_BT above the band splitting, and no difference is found between the results obtained for different Sn amounts.

D. Power factor

The power factor $PF(T) = S^2(T)\sigma(T)$ was calculated using S as in Sec. IV C. As a result, one can notice (Fig. 7) that PF exhibits the largest values at higher temperature for samples with higher nominal carrier concentrations. PF may reach almost 4 W m^{-1} K^{-2} $\times$ 10^{-3} for $n \sim 6 \times 10^{20}$ cm^{-3} at $T \sim 800$ K.

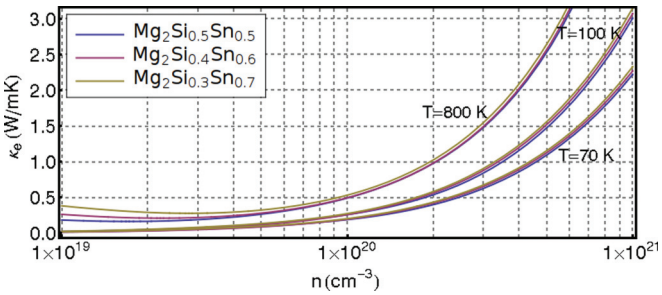

FIG. 8. (Color online) Electronic part of the thermal conductivity κ_e as a function of nominal concentration for three different temperatures.

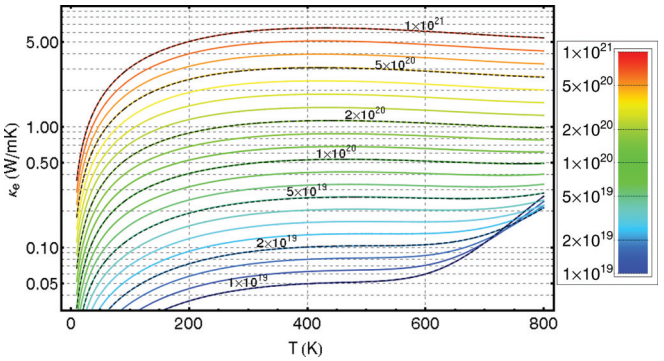

FIG. 9. (Color online) Electronic part of the thermal conductivity κ_e of $Mg_2Si_{0.4}Sn_{0.6}$ in logarithmic scale as a function of temperature for different nominal concentrations (concentration values given by the color in the legend).

E. Electronic thermal conductivity

The electronic part of the thermal conductivity $\kappa_e = \kappa_e(T,n)$ was determined using the same lifetime $\tau_0(T)$ as for electrical conductivity σ (also any variation of τ with carrier concentration was neglected). Figure 8 shows an exponential increase of κ_e as a function of nominal concentration (in logarithmic scale), which means that κ_e is proportional to the nominal concentration at a given temperature ($\kappa_e \sim n$). Differences between various alloys are noticeable mostly at low concentration and high temperature. The rise of κ_e caused by thermally activated electrons crossing the energy gap can be noticed. Consequently, the largest increase of electronic thermal conductivity is detected for $Mg_2Si_{0.3}Sn_{0.7}$, where the smallest gap of the investigated compositions ($x = 0.5$, 0.6, 0.7) was found.

Figure 9 shows that $\kappa_e(T)$ remains almost constant for $T >$ 200 K. In addition, quite regular distance between neighboring thermal conductivity curves at a given temperature is worth noting. This feature also supports the linear relation between κ_e and n (logarithmic scale in value as well as in concentration).

F. Lorenz number

The calculation of both electrical conductivity and the electronic part of the thermal conductivity as a function of

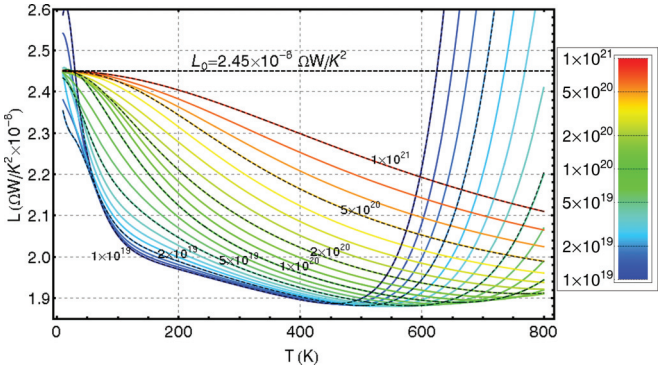

FIG. 10. (Color online) Effective Lorenz number of $Mg_2Si_{0.4}Sn_{0.6}$ as a function of temperature for different nominal concentrations (concentration values given by the color in the legend). The dashed horizontal line denotes the metallic limit.

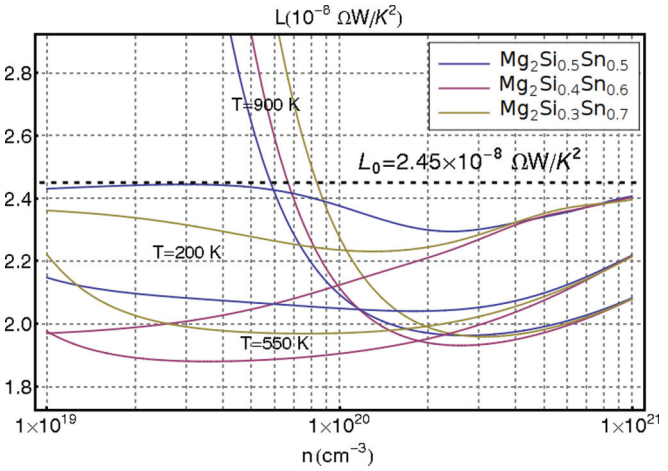

FIG. 11. (Color online) Effective Lorenz number as a function of nominal concentration for three different compounds and temperatures. The dashed horizontal line denotes the metallic limit.

temperature allows for investigating the limit of the Wiedemann-Franz law defined by the Lorenz factor $L_0 = \kappa_e/(\sigma T) = \pi^2 k_B^2/(3e) = 2.45 \times 10^{-8}$ W Ω K^{-2}. Indeed, in view of the Sommerfeld model,[16] commonly applied in the metalliclike regime, the Lorenz number is constant and this law is expected to be valid in metals and strongly degenerated semiconductors. In other cases, generalization is needed and $L(T) = \kappa_e(T)/(\sigma(T)T)$ should be treated as an effective quantity.

Figure 10 shows that L varies with temperature and carrier concentration to approach the metallic limit at low temperature and high concentration. On the contrary, at high temperature and low concentration, $L(T)$ substantially increases well above L_0. This behavior is an influence of the band gap affecting $\kappa_e(T)$ more significantly than $\sigma(T)$.

Figure 11 presents $L(n)$ for three different temperatures. At high concentration all effective Lorenz numbers tend to the Sommerfeld limit L_0. At lower concentration $L(n)$ is underestimated except for at high temperature and low concentrations. Such behavior is caused also by the thermal activation of electrons from valence states. Since

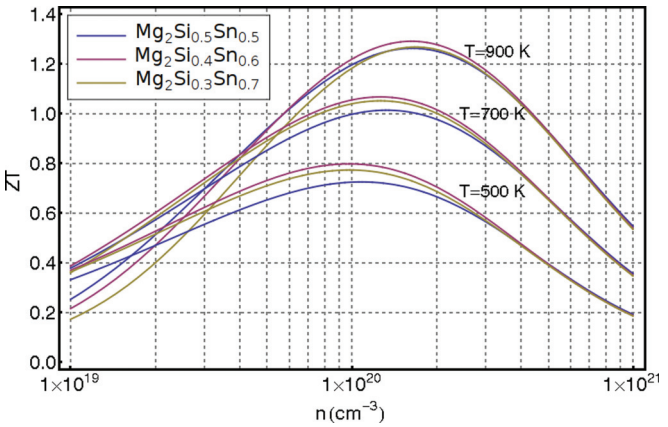

FIG. 12. (Color online) ZT as a function of nominal concentration for three different compounds and temperature, choosing parameter $\kappa_l = 1.25$ W m^{-1} K^{-1}.

$Mg_2Si_{0.3}Sn_{0.7}$ exhibits the smallest gap, the L value becomes highest for small n and high T. This again demonstrates how small gap values have a stronger influence on κ_e than σ. At intermediate temperature (550 K), L is lower than L_0 in a wide range of concentrations. One can examine an interesting case showing that thermal activation of electrons on the one hand is too small to allow for them crossing the gap and, on the other hand, too high to reach Sommerfeld limit L_0, at least for carrier concentration below $n = 1 \times 10^{21}$ cm^{-3}. $Mg_2Si_{0.4}Sn_{0.6}$ has again the lowest value of L (neglecting the high-temperature effect), which makes it the best thermoelectric material of the investigated series of compounds. The effect can be explained only by band degeneracy.

G. ZT

Finally, we attempt to estimate $ZT = S^2\sigma T/(\kappa_e + \kappa_l)$, the dimensionless thermoelectric figure of merit, relying on calculated electron transport properties, i.e., three quantities related to electronic structure (S, σ, κ_e) and one quantity related to crystal lattice dynamics (κ_l). The latter is treated as an adjustable constant parameter, independent of temperature and carrier concentration. In fact, such an assumption seems to be quite reasonable. The measured[21] thermal conductivity shows only small variations (10–20%) in the temperature range 300–800 K. The calculated electronic part also exhibits such behavior (see Fig. 9). Considering κ_l as constant parameter allows for focusing on the direct influence of the electronic band structure on ZT. The lattice part of the thermal conductivity $\kappa_l = 1.25$ W m^{-1} K^{-1} was roughly approximated to an experimental[21] value.

Figure 12 illustrates that ZT of $Mg_2Si_{0.4}Sn_{0.6}$ reaches the largest values in the range of n up to 5×10^{20} cm^{-3}. In addition, the maximum of ZT, as a function of concentration, clearly tends to move to higher values of n when temperature increases. The same behavior is detected in Fig. 13, which shows a two-dimensional map of $ZT(n,T)$ with the color scale from deep blue ($ZT \sim 0.05$) to bright red ($ZT \sim 1.4$). In Table II the largest values of ZT at high temperature and for optimal electron concentrations are listed for $Mg_2Si_{1-x}Sn_x$ with $x = 0.5$, 0.6, and 0.7. ZT has a maximum value (assuming $\kappa_l = 1.25$ W m^{-1} K^{-1}) for electron concentration in the range 1.1–1.6 $\times 10^{20}$ cm^{-3}.

Furthermore, Fig. 14 predicts $ZT(n,T)$ when lattice thermal conductivity is much smaller than the experimentally measured values, but probably available by nanostructural control.[35] On the whole, one can notice that, with the κ_l decrease, the global maximum of ZT moves to a lower temperature and concentration, with ZT reaching values as large as ∼2.

V. CONCLUSIONS

We have shown that electronic-structure KKR-CPA calculations accounting for disorder effects (alloying, doping) combined with the Boltzmann transport approach (employing different models for electron scattering) allow for successfully investigating temperature-dependent transport quantities, which define the thermoelectric figure of merit ZT, i.e., electrical conductivity $\sigma(T)$, thermopower $S(T)$, and thermal conductivity $\kappa = \kappa_e + \kappa_l$ (where κ_l is an adjustable parameter). The aforementioned procedure was implemented to explore

TABLE II. Max ZT at n (10^{20} cm^{-3}) for different concentrations and Sn amounts in $Mg_2Si_{1-x}Sn_x$.

	Max ZT at n ($\times 10^{20}$ cm^{-3})					
	$x = 0.5$		$x = 0.6$		$x = 0.7$	
κ_L (W m^{-1} K^{-1})	600 K	900 K	600 K	900 K	600 K	900 K
0.5	1.55 at 0.69	2.08 at 1.07	1.70 at 0.67	2.10 at 1.13	1.64 at 0.66	2.01 at 1.22
0.75	1.22 at 0.89	1.68 at 1.28	1.32 at 0.84	1.72 at 1.31	1.29 at 0.84	1.67 at 1.39
1	1.02 at 1.05	1.44 at 1.47	1.10 at 0.99	1.47 at 1.48	1.07 at 0.99	1.47 at 1.50
1.25	0.88 at 1.20	1.26 at 1.64	0.94 at 1.11	1.29 at 1.63	0.93 at 1.11	1.27 at 1.68
1.5	0.78 at 1.32	1.13 at 1.80	0.83 at 1.22	1.15 at 1.77	0.82 at 1.22	1.14 at 1.82
1.75	0.70 at 1.43	1.02 at 1.94	0.75 at 1.32	1.05 at 1.90	0.73 at 1.32	1.03 at 1.94
2	0.64 at 1.53	0.94 at 2.07	0.68 at 1.41	0.96 at 2.02	0.67 at 1.41	0.95 at 2.05

n-doped $Mg_2Si_{1-x}Sn_x$, where conduction-band degeneracy appears near $x \sim 0.6$ composition. In comparison with other compositions, i.e., $x = 0.5$ and $x = 0.7$, the KKR-CPA results showed that the band convergence may indeed enhance the thermoelectric properties after appropriate electron doping. We also conclude that the constant lifetime approach well reproduces the temperature-dependent Seebeck coefficient, which remains in excellent agreement with measured $S(T)$. The $ZT(n,T)$ map plotted for $Mg_2Si_{0.4}Sn_{0.6}$ reasonably predicts figures of merit as large as $ZT \sim 1.1$–1.2 in a temperature and carrier concentration range close to that experimentally detected.[21] The ZT values of 1.5–2 in the 600–900 K temperature range are possible if the lattice thermal conductivity can be sufficiently reduced.

ACKNOWLEDGMENTS

We are grateful to Laurent Chaput for useful discussions. This work was supported by the Polish National Science Center (NCN) under Grants No. DEC-2011/02/A/ST3/00124 and No. UMO-2011/03/N/ST3/02644.

APPENDIX: CARRIER MOBILITY IN SEMICONDUCTORS

Originally, carrier mobility referred to a coefficient connecting electrical conductivity with carrier concentration given by the formula $\sigma = e\mu_0 n = e\mu_0 \int d\mathscr{E} f g(\mathscr{E})$. From Eqs. (1), (2), and (3), after averaging the lifetime and velocity of an electron over constant energy surface, the electrical conductivity can be expressed as

$$\sigma(T) = \frac{e^2\langle \tau \mathbf{v}^2 \rangle}{3} \int d\mathscr{E} \left(-\frac{\partial f}{\partial \mathscr{E}} \right) g(\mathscr{E}) = \underbrace{e \frac{\langle \tau \mathbf{v}^2 \rangle}{3} \eta}_{\mu_0} \int d\mathscr{E} f g(\mathscr{E}), \tag{A1}$$

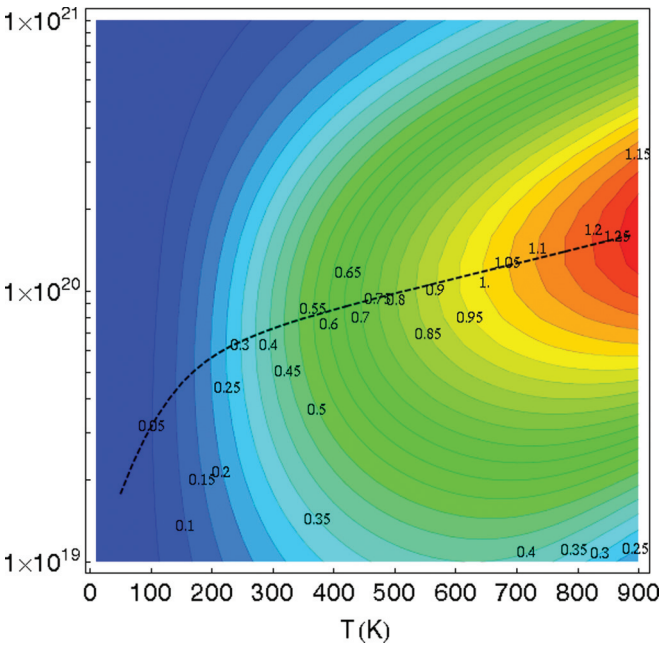

FIG. 13. (Color online) ZT map of $Mg_2Si_{0.4}Sn_{0.6}$ for parameter $\kappa_l = 1.25$ W m^{-1} K^{-1} as a function of temperature and nominal concentration (in cm^{-3}). The black dashed line shows the maximum value of $ZT(n)$.

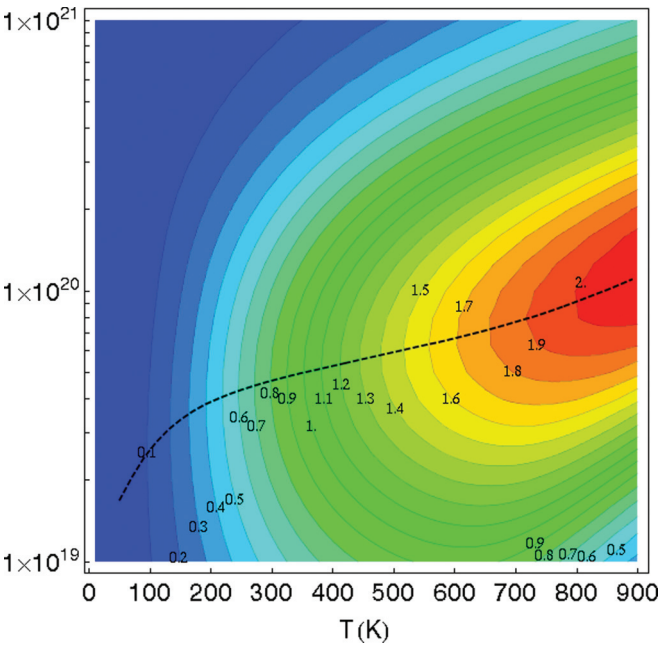

FIG. 14. (Color online) ZT map of $Mg_2Si_{0.4}Sn_{0.6}$ for parameter $\kappa_l = 0.5$ W m^{-1} K^{-1} as a function of temperature and nominal concentration (in cm^{-3}). The black dashed line shows the maximum value of $ZT(n)$.

where

$$\eta = \frac{n_{\text{active}}}{n_{\text{nominal}}} = \frac{k_B T \int d\mathscr{E}\left(-\frac{\partial f}{\partial \mathscr{E}}\right) g(\mathscr{E})}{\int d\mathscr{E}\, f g(\mathscr{E})}. \tag{A2}$$

The $\langle \tau \mathbf{v}^2 \rangle$ is the average over the isoenergetic surface. Note also that for cubic structure $|\mathbf{v} \otimes \mathbf{v}| = 1/3\mathbf{v}^2$. The ratio η in the case of low-doped semiconductors ($n < 1 \times 10^{17}$ cm^{-3}) is 1, but at higher concentration it is usually less than 1 (mostly in low temperature).

[1] T. Thonhauser, T. J. Scheidemantel, J. O. Sofo, J. V. Badding, and G. D. Mahan, Phys. Rev. B **68**, 085201 (2003).
[2] G. K. H. Madsen, K. Schwarz, P. Blaha, and D. J. Singh, Phys. Rev. B **68**, 125212 (2003).
[3] L. Chaput, G. Hug, P. Pécheur, and H. Scherrer, Phys. Rev. B **71**, 121104(R) (2005).
[4] L. Chaput, P. Pécheur, J. Tobola, and H. Scherrer, Phys. Rev. B **72**, 085126 (2005).
[5] I. Mertig, Rep. Prog. Phys. **62**, 237 (1999).
[6] S. Ahmad and S. D. Mahanti, Phys. Rev. B **81**, 165203 (2010).
[7] H. Kohn and N. Rostoker, Phys. Rev. **94**, 1111 (1954).
[8] W. H. Butler, Phys. Rev. B **14**, 468 (1976).
[9] T. Stopa, S. Kaprzyk, and J. Tobola, J. Phys.: Condens. Matter **16**, 4921 (2004).
[10] J. S. Faulkner and G. M. Stocks, Phys. Rev. B **21**, 3222 (1980).
[11] S. Kaprzyk and A. Bansil, Phys. Rev. B **26**, 367 (1982).
[12] S. Kaprzyk and A. Bansil, Phys. Rev. B **42**, 7358 (1990).
[13] A. Bansil, S. Kaprzyk, P. E. Mijnarends, and J. Tobola, Phys. Rev. B **60**, 13396 (1999).
[14] W. H. Butler and G. M. Stocks, Phys. Rev. B **29**, 4217 (1984).
[15] T. Stopa, J. Tobola, S. Kaprzyk, E. K. Hlil, and D. Fruchart, J. Phys.: Condens. Matter **19**, 6379 (2006).
[16] N. W. Ashcroft and N. D. Mermin, *Solid State Physics* (Holt, Rinehart and Winston, New York, 1976).
[17] W. Liu, X. Tang, and J. Sharp, J. Phys. D: Appl. Phys. **43**, 085406 (2010).
[18] P. Zwolenski, J. Tobola, and S. Kaprzyk, J. Electron. Mater. **40**, 889 (2011).
[19] W. H. Fan, R. X. Chen, L. Q. Wang, P. D. Han, and Q. S. Meng, J. Electron. Mater. **40**, 1209 (2011).
[20] V. K. Zaitsev, M. I. Fedorov, E. A. Gurieva, I. S. Eremin, P. P. Konstantinov, A. Y. Samunin, and M. V. Vedernikov, Phys. Rev. B **74**, 045207 (2006).
[21] W. Liu, X. Tan, K. Yin, H. Liu, X. Tang, J. Shi, Q. Zhang, and C. Uher, Phys. Rev. Lett. **108**, 166601 (2012).
[22] J. Tobola, S. Kaprzyk, and H. Scherrer, J. Electron. Mater. **39**, 2064 (2010).
[23] X. J. Tan, W. Liu, H. J. Liu, J. Shi, X. F. Tang, and C. Uher, Phys. Rev. B **85**, 205212 (2012).
[24] Gerald D. Mahan, *Many-Particle Physics*, 3rd ed. (Plenum, New York, 2000).
[25] G. Grimvall, Phys. kondens. Materie **14**, 101 (1972).
[26] J. P. Heremans, B. Wiendlocha, and A. M. Chamoire, Energy Environ. Sci. **5**, 5510 (2011).
[27] W. Liu, Q. Zhang, X. Tang, H. Li, and J. Sharp, J. Electron. Mater. **40**, 1062 (2011).
[28] U. von Barth and L. Hedin, J. Phys. C: Solid State Phys. **5**, 1629 (1972).
[29] P. Lloyd, Proc. Phys. Soc. **90**, 207 (1967).
[30] J. J. Pulikkotil, D. J. Singh, S. Auluck, M. Saravanan, D. K. Misra, A. Dhar, and R. C. Budhani, Phys. Rev. B **86**, 155204 (2012).
[31] Fabien Tran and Peter Blaha, Phys. Rev. Lett. **102**, 226401 (2009).
[32] V. K. Zaitsev, M. I. Fedorov, I. S. Eremin, and E. A. Gurieva, in *Thermoelectrics Handbook: Macro to Nano*, edited by D. M. Rowe (Taylor and Francis, Boca Raton, FL, 2006).
[33] W. E. Lorensen, Comput. Graphics **21**, 4 (1987).
[34] H. Ihou-Mouko, C. Mercier, J. Tobola, G. Pont, and H. Scherrer, J. Alloys Compd. **509**, 6507 (2011).
[35] Kanishka Biswas, Jiaqing He, and Ivan D. Blum, Nature (London) **489**, 414 (2012).